

## Fabrication of Two-Dimensional Photonic Crystal Slab Point-Defect Cavity Employing Local Three-Dimensional Structures

Yoshinori TANAKA\*, Michal TYMCZENKO, Takashi ASANO and Susumu NODA

Department of Electronic Science and Engineering, Kyoto University, Kyoto 615-8510, Japan

(Received February 1, 2006; revised May 26, 2006; accepted May 30, 2006; published online August 4, 2006)

The two-dimensional photonic crystal cavities employing local three-dimensional structures are investigated. Donor-type cavities with small and shallow holes are examined as examples of cavities with a local three-dimensional structure. It is shown that both the far-field and near-field patterns of the cavities can be controlled by the addition of small and shallow holes. The fabrication of such structures using a focused ion beam is proposed and investigated. Residual gallium ions, used in fabrication with a focused ion beam, lead to optical absorption; these gallium ions can be removed by heat treatment at 800 °C. The near-field pattern of a fabricated three-dimensional cavity is measured, and is shown to be consistent with a theoretical analysis. [DOI: 10.1143/JJAP.45.6096]

KEYWORDS: photonic crystal, local three-dimensional structure, focused ion beam, radiation pattern

### 1. Introduction

Point-defect cavities introduced in two-dimensional (2D) photonic crystal (PC) slabs<sup>1–4)</sup> are attracting much attention. They are expected to enable the development of novel devices, such as ultrasmall optical filters,<sup>5,6)</sup> single photon sources,<sup>7)</sup> low-threshold lasers,<sup>8)</sup> and applications in the stopping of light,<sup>9,10)</sup> and the enhancement of nonlinear optics.<sup>11)</sup> In these applications, the characteristics of the cavities, such as the radiation pattern,  $Q$  factor, modal volume and resonant frequency, should be controlled appropriately. Therefore, geometries of the cavities have been modified for the optimization of these characteristics. For this purpose, the shift of the lattice points in the cavity, or the double heterostructure, where the lattice constant of the PC surrounding the cavity is modified, has been investigated.<sup>1–3)</sup> In these cases, note that the designs of the cavity have so far been based only on in-plane parameters.

Vertical structural parameters are also available in the designs of the cavities. Vertical structural parameters include the introduction of shallow holes into the cavities, or the addition of another material on the cavities. The formation of such local three-dimensional (3D) structures allows larger degrees of freedom in the design of the cavities. Therefore, the cavity characteristics including radiation pattern and resonant frequency can be optimized with a higher degree of freedom.

In this study, we investigate the benefits of introducing local 3D structures into the cavities. We focus on the radiation pattern control (both near-field and far-field) of point-defect cavities as a demonstration of the effectiveness of such 3D structures. The fabrication of such local 3D structures using a focused ion beam (FIB) system is also discussed. In §2, we present theoretical investigations of the radiation patterns of the cavities with local 3D structures. In §3, we describe the fabrication of such cavities. In §4, we present measurements of fabricated cavities with local 3D structure, and demonstrate the effect of local 3D structure on the cavity characteristics. Section 5 summarizes the work described in this paper.

### 2. Theoretical Analysis of Local 3D Structure in 2D PC Slabs

We carried out a numerical investigation of local 3D point-defect cavities. The basic structure of the cavities was an L3 donor-type defect<sup>12,13)</sup> introduced into an Si 2D PC slab formed by a triangular lattice of air holes [Fig. 1(a)], with a lattice constant of  $a$ , a slab thickness of  $0.6a$  and an air hole radius of  $0.29a$ . The 3D finite-domain time division (FDTD) method<sup>14)</sup> was used in the analysis, and a perfect matched layer (PML)<sup>15,16)</sup> was introduced as an absorbing boundary.

We discuss three cavities in the following section: a “reference cavity” consisting of an L3 cavity with no local 3D structure [Fig. 1(a)]; “3D cavity A” consisting of an L3 cavity with two shallow holes [Fig. 1(b)]; and “3D cavity B” consisting of an L3 cavity with a single shallow hole [Fig. 1(c)]. The radii of the shallow holes in 3D cavities A and B were set at  $0.29a$ .

#### 2.1 Investigation of far-field pattern

In this section, the far-field pattern of each cavity, which is significant for direct coupling with external optical systems (such as an objective lens and an optical fiber), is investigated.

First, the characteristics of the reference cavity are discussed. The resonant frequency and  $Q$  factor were calculated as  $0.267 c/a$  and 5,200, respectively. The calculated Poynting vector, through the cylindrical surface indicated in Fig. 2(a), is defined as the far-field pattern. The calculated far-field pattern of the reference cavity is shown in Fig. 2(b), normalized by its maximum power. The pattern contains radiation at an angle of about 60° from vertical, in addition to vertical radiation. The fraction of the total power radiated at angles  $|\theta| > 40^\circ$  was calculated as 42.0% [ $\theta$  is defined as shown in Fig. 2(a)].

Second, the characteristics of 3D cavity A are discussed. The resonant frequency of 3D cavity A, with a shallow hole depth of  $0.1a$ , was  $0.269 c/a$ ; this was approximately 0.5% higher than that of the reference cavity owing to the smaller effective refractive index. The  $Q$  factor of the cavity was 750, which is much smaller than that of the reference cavity.

\*E-mail address: ytanaka@qoe.kuee.kyoto-u.ac.jp

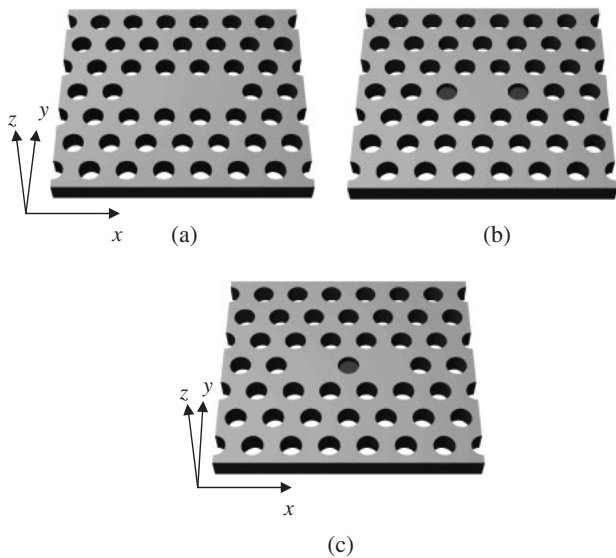


Fig. 1. Schematic diagrams of L3 donor cavities investigated. (a) Reference cavity with no local 3D structures. (b) 3D cavity A with two shallow holes. (c) 3D cavity B with single shallow hole.

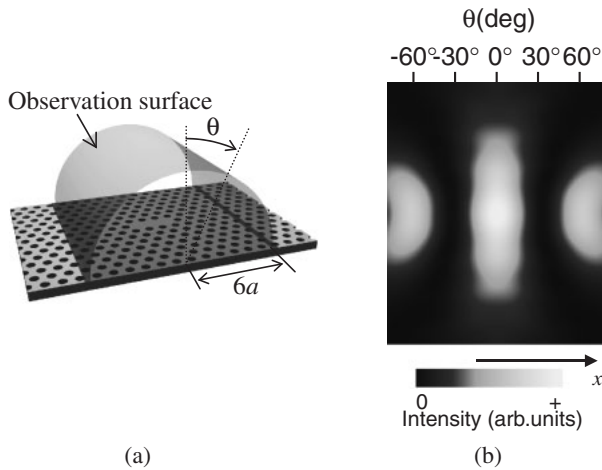


Fig. 2. (a) Observation surface of Poynting vector for far-field pattern. (b) Calculated far-field pattern of reference cavity.

The major origin of the decrease in  $Q$  factor is the transverse electric–transverse magnetic (TE–TM) mode conversion due to structural vertical asymmetry,<sup>17,18)</sup> which can be suppressed by the application of a PC structure having photonic band gap (PBG) for both TE- and TM-like modes.<sup>19)</sup> The calculated far-field pattern of 3D cavity A is shown in Fig. 3(a). This clearly illustrates that the radiation at an angle of about 60° from vertical was suppressed, relative to the reference cavity, and a single-peak pattern was obtained. The power ratio of the far-field component radiated at angles  $|\theta| > 40^\circ$  as a function of shallow hole depth is shown in Fig. 3(b). With an increasing hole depth, the radiation in the vertical direction increases relative to that at angles  $|\theta| > 40^\circ$  and the pattern becomes a single peak. Such a far-field pattern is more useful for connection to optical fibers and lenses than the multippeak pattern of the reference cavity.

Third, the characteristics of 3D cavity B are investigated. The resonant frequency and  $Q$  factor of 3D cavity B, with a shallow hole depth of  $0.1a$ , were calculated as  $0.268 c/a$  and

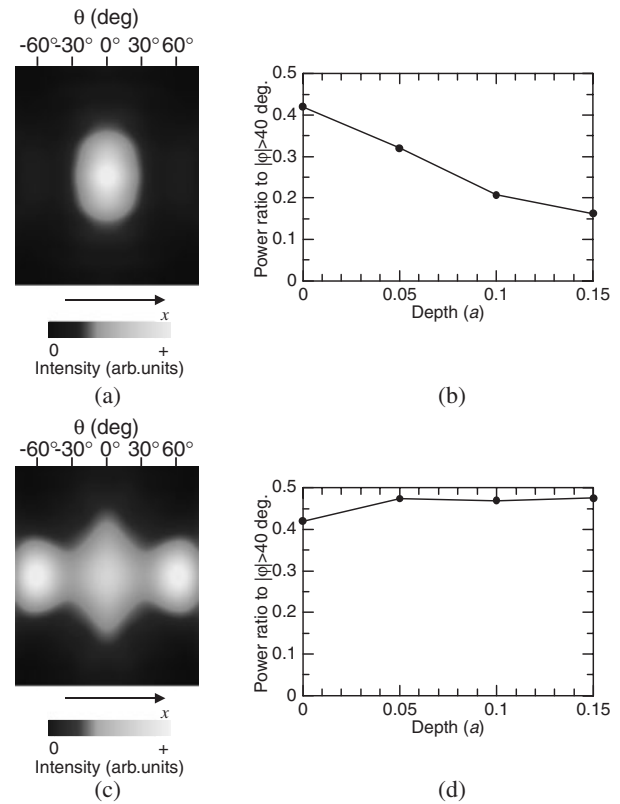


Fig. 3. (a) and (c) calculated far-field patterns of 3D cavity A and 3D cavity B, respectively, with shallow hole depth of  $0.1a$ . (b) and (d) power ratios of the far-field components radiated at angles  $|\theta| > 40^\circ$  from 3D cavity A and 3D cavity B, respectively, as functions of shallow hole depth.

600, respectively. The calculated far-field pattern is shown in Fig. 3(c). The power ratio of the far-field component radiated at angles  $|\theta| > 40^\circ$ , plotted as a function of shallow hole depth, is shown in Fig. 3(d). This indicates that the radiation at 60° to vertical was enhanced, relative to the reference cavity, leading to a broader far-field pattern.

Fourth, the origin of the changes in the far-field patterns is discussed. The introduction of additional shallow holes corresponds to the addition of a dielectric constant perturbation,  $\Delta\varepsilon$ , to the cavity.  $\Delta\varepsilon$  induces coupling between the cavity and radiation modes, which leads to additional radiation from the cavity. There is interference between this additional radiation and the original radiation, which causes the changes in the patterns discussed above.

The additional radiation due to  $\Delta\varepsilon$  can be calculated using the coupled-mode theory. The coupled-mode coefficient  $\kappa(\mathbf{k})$  between the normalized plane wave with wavevector  $\mathbf{k}$  and the cavity mode is given by

$$\kappa(\mathbf{k}) = \frac{\omega\varepsilon_0}{4} \iiint \Delta\varepsilon \mathbf{E}_{\text{cav}} \mathbf{E}_{\text{rad}}^*(\mathbf{k}) dx dy dz, \quad (1)$$

where  $\mathbf{E}_{\text{cav}}$  is the normalized electric field of an unperturbed or reference cavity, and  $\mathbf{E}_{\text{rad}}(\mathbf{k})$  is the electric field of a plane wave with a wavevector of  $\mathbf{k}$ .  $\mathbf{E}_{\text{rad}}(\mathbf{k})$  is normalized by the Poynting power per unit area. The electromagnetic field changes,  $\Delta\mathbf{E}$  and  $\Delta\mathbf{H}$ , caused by  $\Delta\varepsilon$  are given by

$$\Delta\mathbf{E} = \int_{|\mathbf{k}|=k_0} -j\kappa(\mathbf{k}) \mathbf{E}_{\text{rad}}(\mathbf{k}) d\mathbf{k} \quad (2)$$

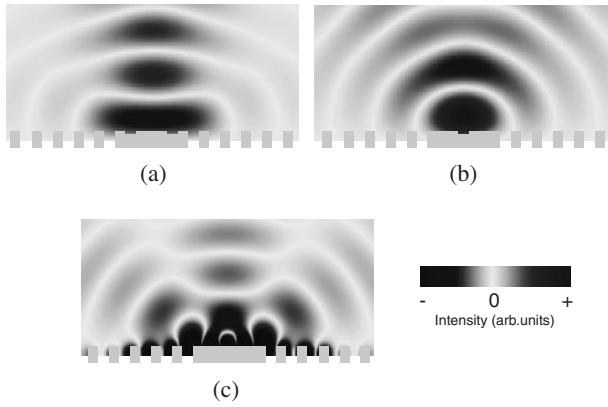


Fig. 4. (a) and (b) Electric field change  $\Delta E$  due to the dielectric constant perturbation  $\Delta \epsilon$  calculated using coupled-mode theory: (a) 3D cavity A; (b) 3D cavity B. (c) Electric field of an unperturbed (reference) cavity.

and

$$\Delta \mathbf{H} = \int_{|\mathbf{k}|=k_0} -j\kappa(\mathbf{k})\mathbf{H}_{\text{rad}}(\mathbf{k}) d\mathbf{k}. \quad (3)$$

$\Delta \mathbf{E}$  and  $\Delta \mathbf{H}$  were calculated using eqs. (1)–(3), where  $\mathbf{E}_{\text{cav}}$  and  $\mathbf{H}_{\text{cav}}$  are obtained from 3D FDTD calculations. Figures 4(a) and 4(b) show the  $\Delta \mathbf{E}$ s of 3D cavity A and 3D cavity B, respectively, in the  $x$ - $z$  plane through the center of the cavity. Figure 4(c) shows the  $\mathbf{E}_{\text{cav}}$  of an unperturbed or reference cavity in the same  $x$ - $z$  plane. The additional radiation from 3D cavity A is emitted over a narrow range of angles perpendicular to the slab, whereas the additional radiation from 3D cavity B is emitted over a broad range of angles; these differences lead to the changes in the far-field pattern, relative to that of the reference cavity, shown in Figs. 3(a) and 3(c).

### 2.2 Investigation of near-field pattern

The control of the near-field pattern of a point-defect cavity is interesting. Here, the near-field patterns of cavities observed through a typical objective lens, with a numerical aperture (NA) of 0.4, are discussed.

The near-field pattern observed through the objective lens is discussed in the wave-number region. Figure 5(a) shows the 2D Fourier transform of the electric-field distribution of the cavity mode of the reference cavity on the surface of the slab obtained by the 3D FDTD method. The solid circle indicates the light line—only light inside this is radiated to free space. Furthermore, when the near-field pattern is observed from the vertical direction ( $\varphi = 0^\circ$ ; Fig. 5(b)), the component observable through the lens can be given by

$$k_x^2 + k_y^2 < (k_0 \sin \psi)^2, \quad (4)$$

where  $k_0$  is the wavenumber in the free space at the cavity resonant frequency and  $\psi$  is the half angle of the cone of light accepted by the lens.  $\psi$  satisfies  $\sin \psi = \text{NA}$ . The observable component calculated from eq. (4) corresponds to the components inside the dashed circle in Fig. 5(a). The near-field pattern observed through the lens can be calculated by the inverse Fourier transformation of the component inside the red dashed circle. The calculated near-field pattern for  $\varphi = 0^\circ$  is shown in Fig. 5(c); a single-peak pattern was obtained. When the near-field pattern was observed from a

direction inclined to the  $x$ - $z$  plane,  $\varphi \neq 0^\circ$ , the observable component in the wave-number region can be given by (see Appendix)

$$\frac{(k_x - k_0 \sin \varphi \cos \psi)^2}{(k_0 \cos \varphi \sin \psi)^2} + \frac{k_y^2}{(k_0 \sin \psi)^2} < 1. \quad (5)$$

The component observed through the lens when  $\varphi = 26^\circ$ , for example, is inside the dashed ellipse in Fig. 5(a). The near-field patterns in the case of  $\varphi \neq 0^\circ$  can be calculated by the inverse Fourier transformation of the component observed through the lens. The calculated near-field patterns for  $\varphi = 10, 20,$  and  $26^\circ$  are shown in Figs. 5(d)–5(f), respectively. The figures show that the near-field pattern for  $\varphi = 20^\circ$  was elliptical, and that the pattern for  $\varphi = 26^\circ$  was multipeak.

Similar calculations were carried out for 3D cavity A, with a shallow hole depth of  $0.1a$ . The 2D Fourier transform of the electric field at the slab surface is shown in Fig. 6(a). The near-field patterns for  $\varphi = 0, 10, 20,$  and  $26^\circ$  were calculated by the same method as that used for the reference cavity. The calculated near-field patterns are shown in Figs. 6(b)–6(e), respectively. The results clearly show that 3D cavity A has a single-peak near-field pattern, even for  $\varphi = 26^\circ$ .

Such changes in the near-field pattern are due to changes in the dielectric constant perturbation  $\Delta \epsilon$ . To demonstrate this, the electromagnetic-field distribution on the slab surface of the 3D cavity A is calculated from  $\Delta \epsilon$  and the electromagnetic field of the reference cavity using eqs. (1)–(3). The near-field patterns are calculated from the obtained electromagnetic field on the surface obtained from eqs. (1)–(3) using the Fourier and the inverse Fourier transforms described before. Figure 7 shows the calculated near-field pattern and is consistent with Fig. 6, which was obtained by the direct 3D FDTD method. These results show that the near-field pattern of a 2D PC slab cavity can be controlled by manipulating the local 3D structure.

### 3. Fabrication of 2D PC Cavities with Local 3D Structure

In the previous section, we theoretically analyzed 2D PC point-defect cavities with local 3D structures, and showed that both the near-field pattern and the far-field pattern can be controlled by the local 3D structure. Several fabrication processes are available to fabricate 2D PC point-defect cavities with local 3D structures, such as plasma processes, FIB and nano-manipulation systems. In this section, we discuss the fabrication of 2D PC slab cavities with local 3D structures using FIB.

FIB irradiates a focused gallium ion beam to the sample, which sputters the surface; FIB can be used to introduce shallow and small holes. The spot size of the gallium ion beam is on the order of several nanometers, so structures can be made with a resolution of 10 nm. The sample surface can be observed by secondary electron images generated from the gallium ions in the FIB system, which allows the positional control of the fabrication process. There have been several reports on applying FIB to the fabrication of 2D PCs, such as that of a 2D PC waveguide fabricated by FIB<sup>20)</sup> and that of a small 2D PC introduced into a ridge waveguide by FIB.<sup>21)</sup> However, one drawback of this process is that the remaining gallium ions in the PC slab absorb light and lead

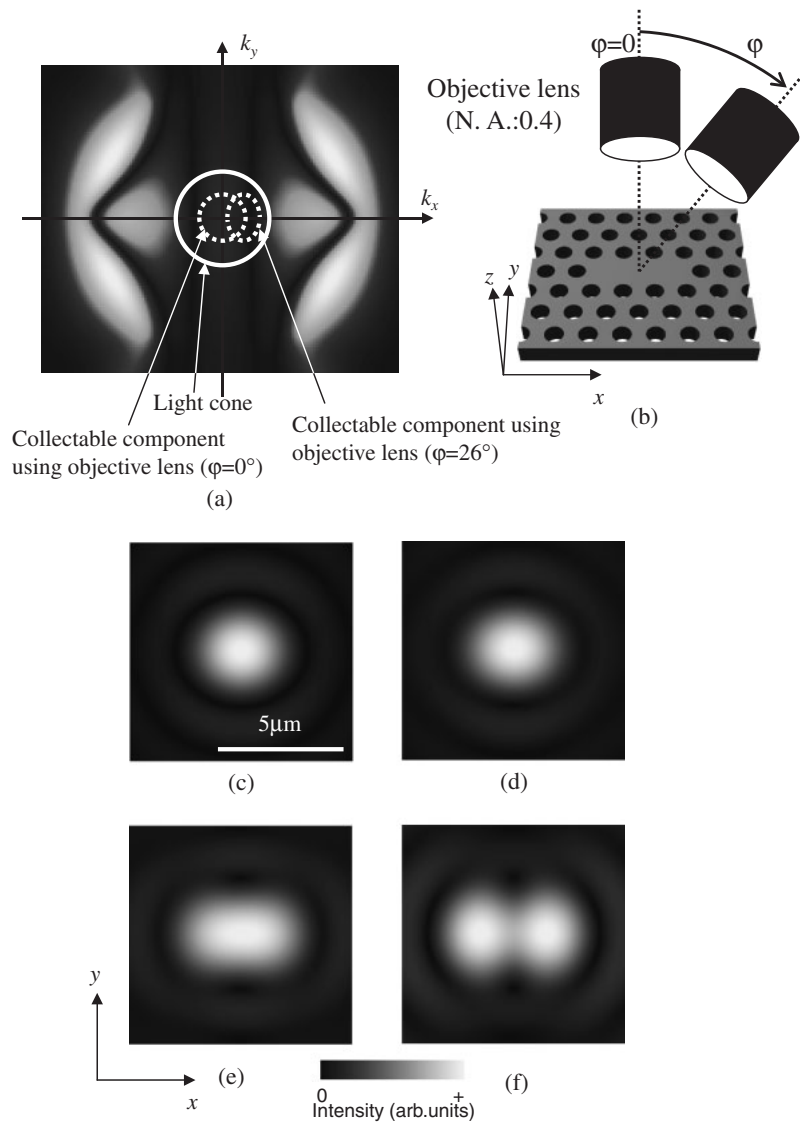


Fig. 5. (a) 2D Fourier transform of electric-field distribution of reference cavity mode on slab surface. The solid red circle indicates the light line and the dashed red circle indicates the component collectable using the objective lens. (b) Schematic of observation of near-field pattern from oblique direction at angle  $\varphi$ . (c)–(f) Calculated near-field patterns of reference cavity, with  $\varphi = 0, 10, 20,$  and  $26^\circ$ , respectively.

to a decrease in  $Q$  factor. In particular, if the FIB process is applied to the cavity, the absorption of the cavity is critical compared with that of the waveguide, as the light remains for a longer time in the cavity. Therefore, the influence of residual gallium ions was investigated, and is discussed below.

In the fabrication of 3D cavity A, with shallow hole depths of  $0.1a$  using FIB, the number of gallium ions required was estimated to be  $6.2 \times 10^7$ . We assumed that all the irradiated gallium ions remained in the silicon slab. The cavity volume was approximately  $3 \times 10^{-19} \text{ cm}^3$  and the number of silicon atoms in the cavity was  $1.2 \times 10^{10}$ . Therefore, the fraction of gallium atoms was estimated to be 0.5%. The absorption coefficient of metal gallium,  $\alpha$ , is  $4.2 \times 10^6 \text{ cm}^{-1}$  at a wavelength of  $1.5 \mu\text{m}$ .<sup>22)</sup> The absorption coefficient of the Si slab with the irradiated gallium ions was calculated to be  $2.1 \times 10^4 \text{ cm}^{-1}$ . The relationship between  $Q$  factor and absorption coefficient  $\alpha$  is given by

$$Q = \omega n / \alpha c, \tag{6}$$

as the time evolution of the stored energy in a cavity can be described as  $\exp(-\omega t / Q)$  and the propagation loss can be described as  $\exp(-\alpha z) = \exp(-\alpha ct / n)$ , where  $z$ ,  $c$ , and  $n$  are the mean propagation length, the velocity of light in vacuum and the refractive index of the slab, respectively. The  $Q$  factor calculated from eq. (6), determined by the optical absorption of gallium ions, was 7.2; this is much smaller than the  $Q$  factor of the cavity calculated by the 3D FDTD method assuming that the material has no optical absorption. Therefore, the  $Q$  factors of cavities fabricated using FIB will be determined by the optical absorption of the residual gallium ions.

To avoid the influence of optical absorption by gallium ions, the sample can be heat treated. The diffusion and evaporation of gallium ions from the cavity during heat treatment are expected. To evaluate the effect of heat treatment, silicon-on-insulator (SOI) substrates irradiated with  $8.0 \times 10^{15} \text{ cm}^{-2}$  gallium ions onto a  $1 \times 1 \text{ mm}^2$  region were heat treated in vacuum for 2 h at several different temperatures. The number of gallium ions remaining was

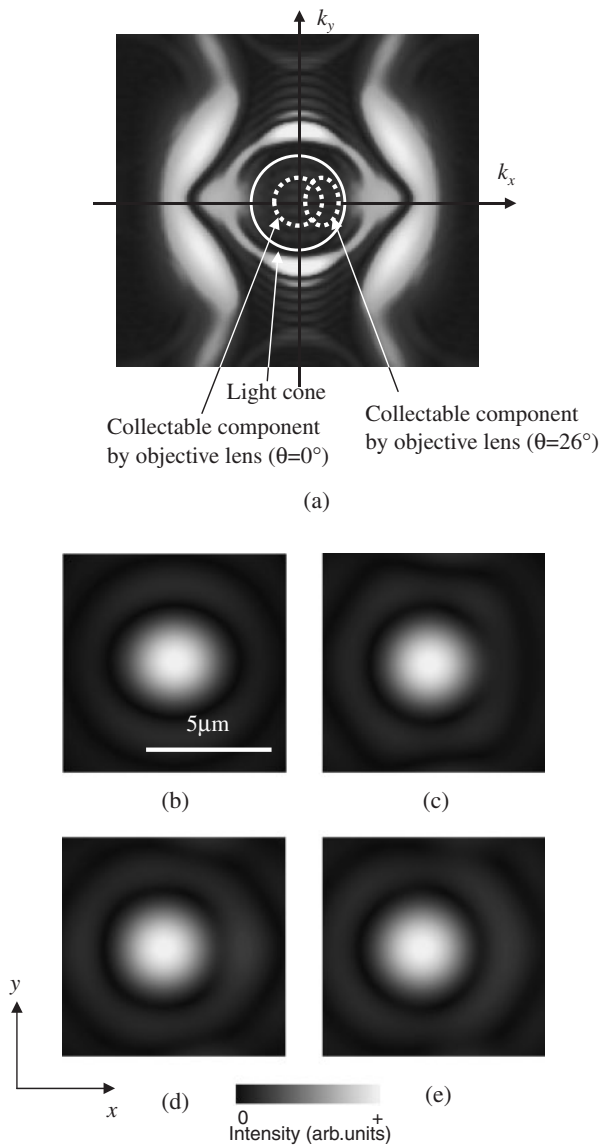


Fig. 6. (a) 2D Fourier transform of electric-field distribution of the cavity mode of 3D cavity A on slab surface obtained from 3D FDTD calculation. The solid red circle indicates the light line and the dashed red circle indicates the collectable angle of the objective lens. (b)–(e) Calculated near-field patterns of 3D cavity A from electric field obtained from 3D FDTD calculations, with  $\varphi = 0, 10, 20,$  and  $26^\circ$ , respectively.

evaluated by energy dispersive X-ray spectroscopy (EDS). The ratio of the number of gallium atoms to the number of silicon atoms as a function of heating temperature is shown in Fig. 8. The data show that heat treatment at  $800^\circ\text{C}$  can reduce the number of gallium ions to less than one-fiftieth their original concentration (under the measurement limit). Therefore, with this treatment, optical absorption due to the remaining gallium ions is expected to be reduced.

Using these results, we fabricated point-defect cavities in 2D PC slabs with local 3D structures using FIB. A 2D PC pattern with L3 point defects was introduced by electron-beam lithography and induction-coupled plasma (ICP) dry etching into the silicon layer of the SOI substrate. The lattice constant and air hole radius were set as 420 and 120 nm, respectively. Then, local 3D structures were introduced into the cavity by FIB, followed by heat treatment at  $800^\circ\text{C}$  in vacuum for 2 h. The  $\text{SiO}_2$  layer under the PC slab was

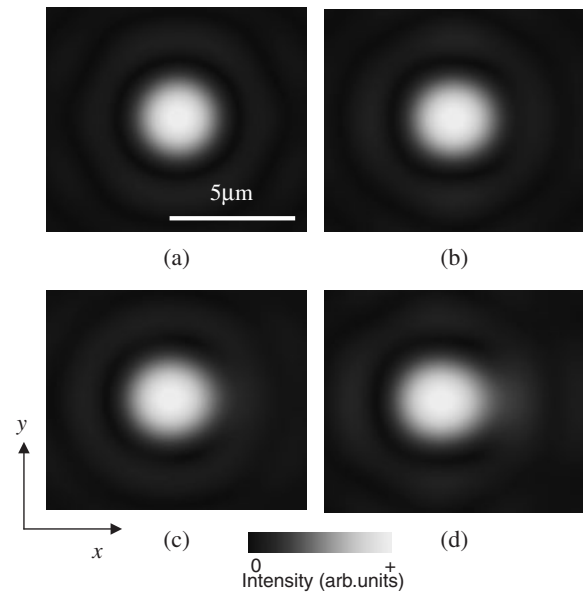


Fig. 7. Calculated near-field patterns of 3D cavity A from electric field obtained from coupled-mode theory; (a)–(d) correspond to  $\varphi = 0, 10, 20,$  and  $26^\circ$ , respectively.

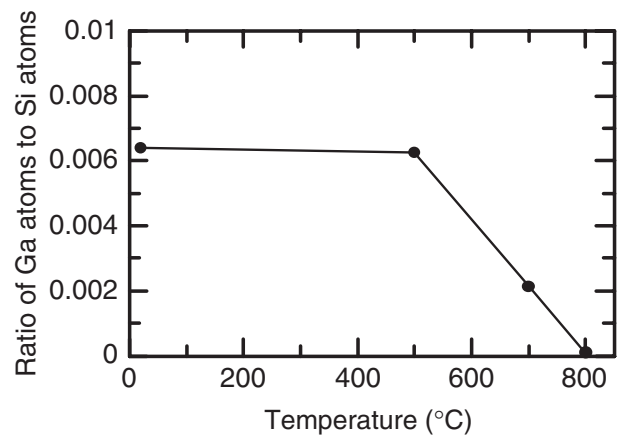


Fig. 8. Ratio of gallium atoms to silicon atoms in SOI substrate irradiated with  $8.0 \times 10^{15} \text{ cm}^{-2}$  gallium atoms, as function of heat treatment temperature; measured by EDS.

removed by HF wet etching after the heating process. A scanning electron microscopy (SEM) image of fabricated 3D cavity A is shown in Fig. 9(a), which indicates that shallow holes with a radius of 120 nm and a depth of 40 nm were successfully introduced into the L3 cavity. A line defect waveguide was set near each cavity to introduce light by evanescent coupling. The spectra of the cavities were obtained by introducing light from a tunable laser into the waveguide and by detecting the radiation from the cavity to free space. The observed spectra of fabricated 3D cavity A, produced with and without heat treatment, are shown in Fig. 9(b). The spectra demonstrate that radiation to free space can be obtained from a cavity with heat treatment, but not from a cavity without heat treatment. This result clearly shows that irradiated gallium ions are successfully removed by heat treatment. These results reveal that cavities with 3D structures introduced using FIB can be operated after heat treatment at  $800^\circ\text{C}$  in vacuum for 2 h.

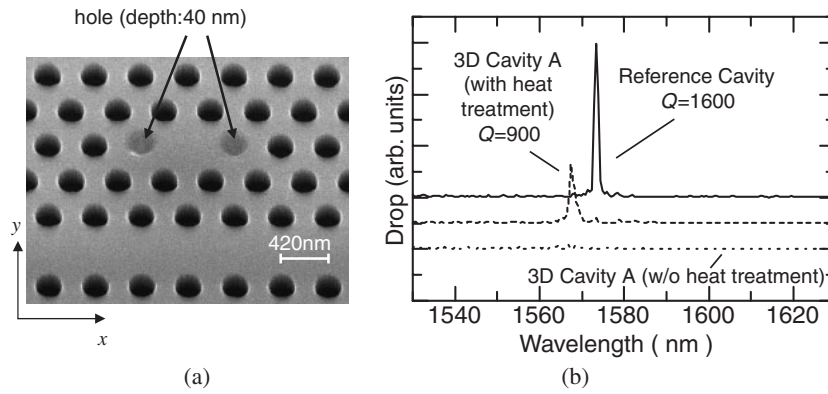


Fig. 9. (a) SEM image of fabricated 3D cavity A. (b) Measured spectra of 3D cavity A with and without heat treatment, and that of reference cavity.

#### 4. Experimental Observation of Near-Field Pattern of Cavity with Local 3D Structure

As discussed in §2, both the far-field patterns and near-field patterns of point-defect cavities in 2D PC slabs can be controlled by introducing small and shallow holes into the cavities. In §3, we discussed the fabrication of shallow holes into 2D PC slab point-defect cavities using FIB. In this section, we describe the near-field pattern of a fabricated 2D PC cavity with local 3D structures.

The resonant wavelength of 3D cavity A shown in Fig. 9 was approximately 6 nm shorter than that of the reference cavity, because the average refractive index of the cavity was decreased by the shallow holes. The  $Q$  factor and radiation intensity of 3D cavity A were approximately one-half and one-third of those of the reference cavity, respectively. These decreases are due to the TE–TM coupling arising from the structural vertical asymmetry, and are consistent with the calculations presented in §2.

We observed the near-field patterns of the fabricated reference cavity and fabricated 3D cavity A. We prepared the point defect cavity and line defect waveguide nearby as shown in Fig. 9(a) and light from a tunable laser is introduced into the cavity via the waveguide. A schematic image of the measurement system is shown in Fig. 10. The sample is set at an angle of  $\varphi$  against the optical axis of lens A in the  $x$ – $z$  plane. Figure 11 shows the observed near-field patterns of the reference cavity through the objective lens B with  $NA = 0.4$ . The patterns became elliptical as  $\varphi$  was increased and a multipeak pattern was obtained when  $\varphi = 26^\circ$ . Figure 12 shows the observed near-field patterns of 3D cavity A; a single-peak near-field pattern was obtained even when  $\varphi = 26^\circ$ . These results are consistent with the theoretical results presented in §2.2 and provide experimental evidence of the effects of 3D structure, produced using FIB, on point-defect cavities.

#### 5. Conclusions

We have proposed the introduction of local 3D structures into a point-defect cavity in a 2D PC slab. In this study, we have investigated the near-field and far-field patterns of L3 donor cavities in a 2D PC slab with small and shallow holes, both theoretically and experimentally. We have revealed that both near-field and far-field patterns can be controlled by local 3D structure in the cavity. In particular, we have shown

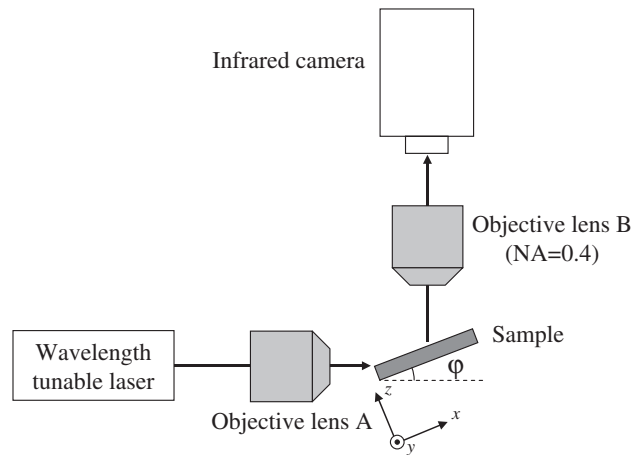


Fig. 10. Schematic image of measurement system for near-field patterns from inclined direction.

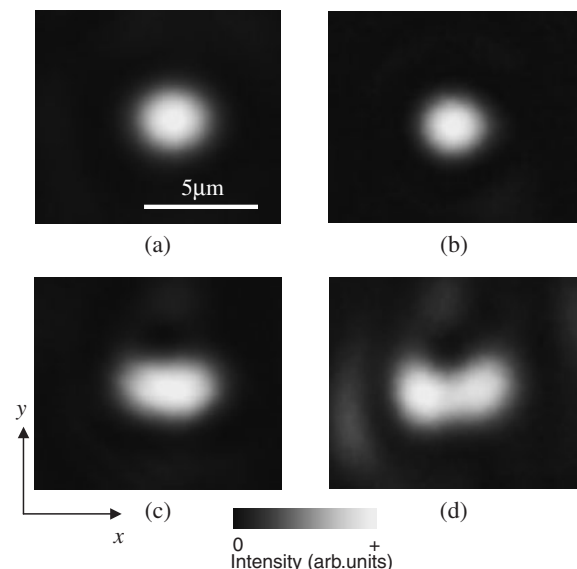


Fig. 11. Measured near-field patterns of reference cavity; (a)–(d) correspond to  $\varphi = 0, 10, 20,$  and  $26^\circ$ , respectively.

that a cavity with two shallow holes (3D cavity A) has a single-peak near-field pattern and a single-peak far-field pattern. We have also discussed the fabrication of such local 3D structures using FIBs. We have revealed that the

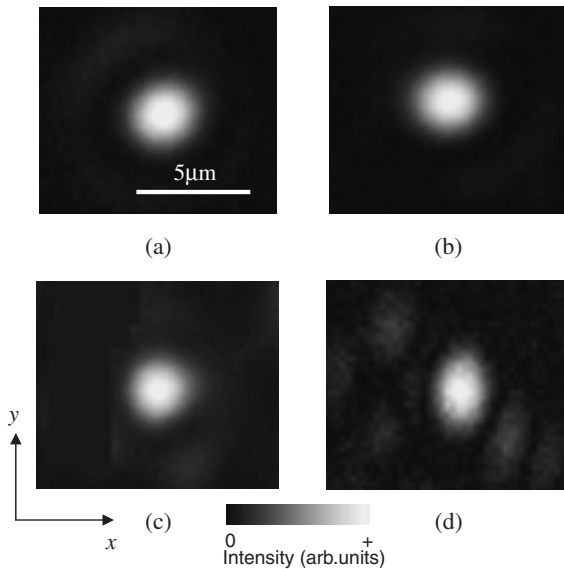


Fig. 12. Measured near-field patterns of 3D cavity A; (a)–(d) correspond to  $\varphi = 0, 10, 20,$  and  $26^\circ$ , respectively.

pollution of PCs by gallium ions in the local 3D structure fabrication process leads to optical absorption, but that the gallium ions can be removed by heat treatment. The experimental near-field pattern of 3D cavity A, fabricated by FIB described in this paper, has a single peak, in agreement with theoretical results. The methods of theoretical analyses and the fabrication process described in this paper can be applied not only to the control of the near-field and far-field patterns, but also to other designs of point defect cavity characteristics, such as the radiation ratio in upward and downward directions, and the local addition of nonlinear or active materials into 2D PC slab cavities.

### Acknowledgments

This work was partly supported by a Grant-in-Aid for Scientific Research from the Ministry of Education, Culture, Sports, Science and Technology of Japan. Y. Tanaka was supported by a Research Fellowship of the Japan Society for the Promotion of Science.

### Appendix

The component accepted through the lens in the case of the observation from a direction inclined to the  $x$ – $z$  plane at an angle of  $\varphi$  is discussed. A Fourier component of the cavity mode with a wave vector of  $(k_x, k_y)$  can couple to the

free space mode with a wave vector of  $\mathbf{k} = (k_x, k_y, \sqrt{k_0^2 - k_x^2 - k_y^2})$  when the Fourier component is inside the light cone, where  $k_0$  is the wave vector in the free space at the cavity resonant frequency. When the free space mode is accepted in the lens, the angle between the free space mode  $\mathbf{k}$  and the unit vector parallel to the optical axis of the objective lens  $\mathbf{e}_{\text{lens}} = (\sin \varphi, 0, \cos \varphi)$  is less than  $\psi$ , where  $\psi$  is the half angle of the cone of light accepted by the lens.  $\psi$  satisfies  $\sin \psi = \text{NA}$ . Therefore,  $\mathbf{k}$  and  $\mathbf{e}_{\text{lens}}$  satisfy

$$\frac{\mathbf{k} \cdot \mathbf{e}_{\text{lens}}}{|\mathbf{k}| |\mathbf{e}_{\text{lens}}|} > \cos \psi, \quad (\text{A}\cdot 1)$$

and eq. (5) can be derived from eq. (A.1).

- 1) Y. Akahane, T. Asano, B. S. Song and S. Noda: *Nature* **425** (2003) 944.
- 2) B. S. Song, S. Noda, T. Asano and Y. Akahane: *Nat. Mater.* **4** (2005) 207.
- 3) T. Asano, B. S. Song and S. Noda: *Opt. Express* **14** (2006) 1996.
- 4) T. Yoshie, J. Vučković, A. Scherer, H. Chen and D. Deppe: *Appl. Phys. Lett.* **79** (2001) 4289.
- 5) S. Noda, A. Chutinan and M. Imada: *Nature* **407** (2000) 608.
- 6) B. S. Song, S. Noda and T. Asano: *Science* **300** (2003) 1537.
- 7) P. Michler, A. Kiraz, C. Becher, W. V. Schoenfeld, P. M. Petroff, L. Zhang, E. Hu and A. Imamoglu: *Science* **290** (2000) 2282.
- 8) O. Painter, R. K. Lee, A. Scherer, A. Yariv, J. D. O'Brien, P. D. Dapkus and I. Kim: *Science* **284** (1999) 1819.
- 9) M. F. Yanik and S. Fan: *Phys. Rev. Lett.* **92** (2004) 083901.
- 10) M. F. Yanik and S. Fan: *Phys. Rev. A* **71** (2005) 013803.
- 11) S. M. Spillane, T. J. Kippenberg and K. J. Vahala: *Nature* **415** (2002) 621.
- 12) Y. Akahane, M. Mochizuki, T. Asano, Y. Tanaka and S. Noda: *Appl. Phys. Lett.* **82** (2003) 1341.
- 13) Y. Akahane, T. Asano, B. S. Song and S. Noda: *Appl. Phys. Lett.* **83** (2003) 1512.
- 14) K. S. Yee: *IEEE Trans. Antennas Propag.* **14** (1966) 302.
- 15) J. P. Berenger: *J. Comput. Phys.* **114** (1994) 185.
- 16) M. Okano, S. Kako and S. Noda: *Phys. Rev. B* **68** (2003) 235110.
- 17) Y. Tanaka, T. Asano, Y. Akahane, B. S. Song and S. Noda: *Appl. Phys. Lett.* **82** (2003) 1661.
- 18) Y. Tanaka, T. Asano, R. Hatsuta and S. Noda: *Appl. Phys. Lett.* **88** (2006) 011112.
- 19) S. Takayama, H. Kitagawa, Y. Tanaka, T. Asano and S. Noda: *Appl. Phys. Lett.* **87** (2005) 061107.
- 20) M. Nakao, S. Oku, H. Tanaka, Y. Shibata, A. Yokoo, T. Takamura and H. Masuda: *Opt. Quantum Electron.* **34** (2002) 183.
- 21) S. Cabrini, A. Carpentiero, R. Kumar, L. Businaro, P. Candeloro, M. Prasciolu, A. Gosparini, C. Andreani, M. De Vittorio, T. Stomeo and E. Di Fabrizio: *Microelectron. Eng.* **78–79** (2005) 11.
- 22) *Landolt-Börnstein, New Series*, ed. K. H. Hellerge and O. Madelung (Springer-Verlag, Berlin, 1985) Vol. 15, Subvol. b, p. 216.